



ISTITUTO NAZIONALE DI RICERCA METROLOGICA Repository Istituzionale

A new analysis for diffraction correction in optical interferometry

Original

A new analysis for diffraction correction in optical interferometry / Mana, G; Massa, E; Sasso, C. P; Andreas, B; Kuetgens, U.. - In: METROLOGIA. - ISSN 0026-1394. - 54:4(2017), pp. 559-565. [10.1088/1681-7575/aa76af]

Availability:

This version is available at: 11696/56845 since: 2020-05-25T09:05:18Z

Publisher:

IOP

Published

DOI:10.1088/1681-7575/aa76af

Terms of use:

This article is made available under terms and conditions as specified in the corresponding bibliographic description in the repository

Publisher copyright

(Article begins on next page)

A new analysis for diffraction correction in optical interferometry

This content has been downloaded from IOPscience. Please scroll down to see the full text.

2017 Metrologia 54 559

(<http://iopscience.iop.org/0026-1394/54/4/559>)

View [the table of contents for this issue](#), or go to the [journal homepage](#) for more

Download details:

IP Address: 5.170.4.36

This content was downloaded on 18/07/2017 at 14:35

Please note that [terms and conditions apply](#).

A new analysis for diffraction correction in optical interferometry

G Mana¹ , E Massa¹, C P Sasso¹, B Andreas² and U Kuetgens²

¹ INRIM—Istituto Nazionale di Ricerca Metrologica, Str. delle Cacce 91, 10135 Torino, Italy

² PTB—Physikalish Technische Bundesanstalt, Bundesalle 100, 38116 Braunschweig, Germany

E-mail: g.mana@inrim.it

Received 31 March 2017, revised 19 May 2017

Accepted for publication 2 June 2017

Published 18 July 2017



CrossMark

Abstract

Dimensional measurements by laser interferometry require a correction because of diffraction, which makes the fringe period different from the wavelength of a plane wave. The fractional correction—from parts in 10^{-7} to parts in 10^{-9} , depending on the beam collimation—is half the central second moment of the angular power-spectrum of the beam, a generalization of the divergence concept. We report new insights into the second moment measurement and their consequences on the measurement of the silicon lattice parameter by combined x-ray and optical interferometry.

Keywords: interferometers, silicon lattice parameter, diffraction, angular power spectrum

(Some figures may appear in colour only in the online journal)

1. Introduction

The dispersion relation $\lambda = c/\nu$ is valid only for a plane wave. In a laser beam, since the wavefronts bend, the wavelength is different from one point to another and it is different from c/ν . This effect is known as diffraction and is an unavoidable phenomenon connected with the wave nature of light.

Diffraction has been extensively investigated to correct dimensional measurements by laser interferometry [1–14]. When the interfering beams are identical, the detector is infinite, the optical path difference is small, and the displacement to be measured occurs along the beam axis, the fractional difference of the fringe period from the plane wave wavelength is proportional to the divergence square which, for generic paraxial beams, is expressed by the eigenvalues of the second-moment matrix of the angular power-spectrum.

For the dissemination of the unit of length, lasers are calibrated against frequency standards. The frequency calibration achieves relative uncertainties smaller than 10^{-10} , but translating frequency into wavelength requires the characterization of the laser beam and the correction for the effects of

diffraction. By using Gaussian approximations of the interfering beams, the correction is proportional to the divergence square and, typically, ranges from parts in 10^{-7} to parts in 10^{-9} . However, high accuracy measurements and poor beam quality require the determination of the second central moment of the angular power-spectrum, which is the way to generalize the divergence concept to arbitrary paraxial beams. In this paper, we review the angular power spectrum measurement and the basic formulae for the correction calculation and illustrate a new view onto the data analysis, which exploits symmetries to filter the noise without loss of information and to gain visibility of the beam diffraction.

Next, our new view is applied to the INRIM's measurements of the lattice parameter by combined x-ray and optical interferometry [15–17]. These measurements were corrected by imaging the angular power-spectrum in the focal plane of a converging lens [18]. The required accuracy raised questions about the power-spectrum measurements and correction estimates. Recently, a joint INRIM and PTB investigation brought into light the presence of small spectrum components at relatively large angles—consistent with the Airy patterns from diffraction-limited fiber-collimator lenses—that went unnoticed in the previous analyses. Section 4 compares the present and previous data analyses and shows the improvement achieved. The updated corrections are given in section 5.



Original content from this work may be used under the terms of the [Creative Commons Attribution 3.0 licence](https://creativecommons.org/licenses/by/3.0/). Any further distribution of this work must maintain attribution to the author(s) and the title of the work, journal citation and DOI.

2. Theory

2.1. Fourier optics

The angular spectrum of a paraxial beam, $u(x, y; z)e^{ikz}$, which propagates along the z axis with wave-number k ,

$$\tilde{u}(p, q; z) = \frac{1}{2\pi} \iint_{-\infty}^{+\infty} u(x, y; z) e^{-i(px+qy)} dpdq, \quad (1)$$

is its Fourier transform in terms of plane waves with variable propagation directions [5, 19]. In (1), x, y are the transverse coordinates, $p = k\theta_x$ and $q = k\theta_y$, are the reciprocal coordinates, and the $\theta_{x,y}$ angles identify the propagation directions of the plane waves. The beam axis, i.e. the propagation direction of the $u(x, y; z)$ center of mass, π_0 , is identified by the center of mass of the power spectrum $|\tilde{u}(p, q)|^2$. Hence,

$$\pi_0 = \iint_{-\infty}^{+\infty} \pi |\tilde{u}(p, q)|^2 dpdq, \quad (2)$$

where $\pi = (p, q)^T$, the power spectrum is independent of the z coordinate, and we assumed that $u(x, y; z)$ and $\tilde{u}(p, q; z)$ have unit norm. The second central moment is

$$\Gamma_0 = 1/k^2 \iint_{-\infty}^{+\infty} (\pi - \pi_0)(\pi - \pi_0)^T |\tilde{u}(p, q)|^2 dpdq \quad (3)$$

and it generalizes the divergence concept.

2.2. Diffraction correction

In the interference of two identical and coaxial paraxial beams, whose complex amplitudes differ only by free-space propagation, the difference between the period of the interference pattern integrated by an infinite detector, λ_e , and the plane-wave wavelength, $\lambda = 2\pi c/\omega$, is

$$\frac{\lambda_e - \lambda}{\lambda} = \frac{\gamma_1^2 + \gamma_2^2}{2} \quad (4)$$

where the propagation difference is assumed much smaller than the Rayleigh length and $\gamma_{1,2}^2$ are the eigenvalues of the second central moment matrix Γ_0 of the beam angular power spectrum. Equation (4) is the weighted average of each ray cosine-error, it originates from the spread of the transverse impulse of the photons, and it holds for any paraxial beam, no matter if its profile is Gaussian or not. In the case of Gaussian beams having cylindrical symmetry, $\Delta\lambda/\lambda = \theta_0^2/4 = 1/(kw_0)^2$, where $\Delta\lambda = \lambda_e - \lambda$, and θ_0 and $w_0 = 2/(k\theta_0)$ are the beam divergence and the $1/e^2$ radius at the waist.

If the interfering beams are Gaussian, the generalization of (4) to non-coaxial beams,

$$\frac{\lambda_e - \lambda}{\lambda} = \frac{(1 - x_0^2/w_0^2)(\gamma_1^2 + \gamma_2^2)}{2} + \frac{\alpha^2}{2} + \frac{\beta^2}{2}, \quad (5)$$

is given in [7]. In (5), x_0 is the shear of the beam axes at the beam waists, 2α is the misalignment between the beam axes, and β is the angular misalignment between the measurand displacement and the axis of the measurement beam. The $\beta^2/2$ term is of geometrical origin; it expresses that the displacement

occurs at an angle β with respect to the beam axis. The $\alpha^2/2$ and x_0/w_0 terms take the decoupling of the interfering rays, which is due the combination of displacement and spread of the ray bundle, into account.

In order to calculate $\Delta\lambda/\lambda$ by the focal plane method [18], a key observation is that $\gamma_1^2 + \gamma_2^2 = \text{Tr}(\Gamma_0)$, where $\text{Tr}(\Gamma_0)$ is the trace of second moment matrix. Hence, (4) can be rewritten as

$$\frac{\lambda_e - \lambda}{\lambda} = \frac{\text{Tr}(\Gamma_0)}{2}. \quad (6)$$

A second key observation is that the calculation of $\text{Tr}(\Gamma_0)$ requires the integration of the univariate function $\mathcal{I}(\theta)$ resulting from the power-spectrum averaging over the azimuth ϕ of the propagation directions. In fact,

$$\begin{aligned} \text{Tr}(\Gamma_0) &= \int_{-\infty}^{+\infty} \int_{-\infty}^{+\infty} (\theta_x^2 + \theta_y^2) I(\theta) d\theta_x d\theta_y = \int_0^{+\infty} \theta^3 \left[\int_0^{2\pi} I(\theta, \phi) d\phi \right] d\theta \\ &= 2\pi \int_0^{+\infty} \theta^3 \mathcal{I}(\theta) d\theta, \end{aligned} \quad (7)$$

where $I(\theta) = |\tilde{u}(k\theta)|^2$ is the normalized power-spectrum, $\theta = (\theta_x, \theta_y)$ is any propagation direction, and $\theta = |\theta| = \sqrt{\theta_x^2 + \theta_y^2}$ and $\phi = \arctan(\theta_y/\theta_x)$ are elevation and azimuth coordinates in the reciprocal space, whose origin is the beam-axis direction. Equation (7) makes it possible to reduce the noise of the focal plane image, to trace back the identification and elimination of the camera dark-noise to a more tractable one-dimensional fitting problem, and to bring into light spectrum-details otherwise invisible.

3. Combined x-ray and optical interferometry

An x-ray interferometer consists of three Si crystals cut so that the $\{220\}$ diffracting planes are orthogonal to the crystal surfaces [15, 16]. X rays (17 keV Mo K_α source) are split by the first crystal and recombined by the third, which is called the analyser, via a mirror crystal. When the analyser is moved orthogonally to the $\{220\}$ planes, a periodic variation of the transmitted and diffracted x-ray intensities is observed, the period being the diffracting-plane spacing, d . The analyser embeds a front mirror, so that its displacement is measured by optical interferometry. The measurement equation is $d = m\lambda/(2n)$ where n is the number of x-ray fringes in m optical fringes of $\lambda/2$ period.

In 2014, the INRIM made seven measurements of the lattice parameter. Three from February to March, with the interferometer crystals arranged as in the parent ingot (side A). Four from May to June, with the inverted analyser (side B). The measurements, whose accuracy approached $10^{-9}d$, were corrected for the difference between the effective period of the integrated signal and the wavelength of a plane wave. In each measurement campaigns, the angular power-spectrum of the beam emerging from the optical interferometer was measured by using the Fourier transforming properties of a lens. Exemplar results are shown in figure 1.

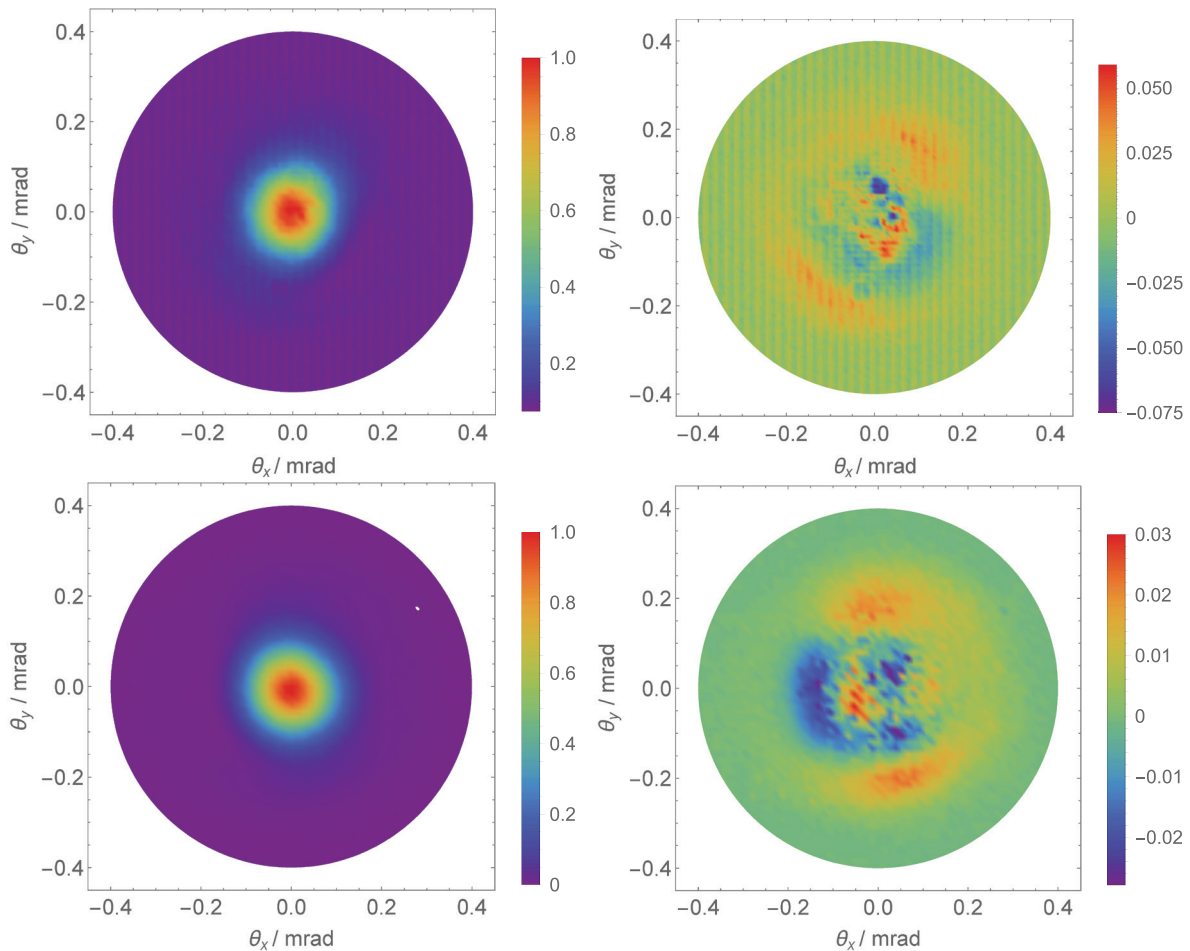


Figure 1. Normalized images of the laser beam. Top: February 2014 measurement, COHU 6710 camera. Bottom: May 2014 measurement, HAMAMATSU FLASH 4.0 camera. Left: focal plane images. Right: residuals after subtracting the dark noise and bivariate Gauss functions. The colours indicate the normalized intensities of the images and residuals.

In February, we used a Hilger and Watts TA3 autocollimator equipped with a COHU 6710 CCD camera; the focal plane calibration was $7.2(2) \mu\text{rad}/\text{pixel}$, but the resolution was limited to 8 bit and the captured images were affected by a large dark noise. The fixed-pattern noise visible in the residuals is due to non-uniformity of the dark currents on the chip; the dark spots are due to dust particles inside the autocollimator.

In May, we used a converging lens having 0.5 m focal length; the focal plane image was acquired by a cooled 16 bit HAMAMATSU CMOS camera FLASH 4.0 having much less readout and dark noises. The focal plane was identified by checking that parallel translations of a laser beam do not cause translations of the beam image; calibration, about $13.3(4) \mu\text{rad}/\text{pixel}$, was accomplished by tilting the beam by known angles. The linear fringe pattern in the residuals—also visible in the February data—might be due to a scratch on the interferometer optics. The rotation between the February and May images is due to the different assembling of the cameras.

4. Data analysis

Up to now, we did not realize that, since it can be expressed in term of $\text{Tr}(\mathbf{\Gamma}_0)$ (which is independent of the $\mathbf{\Gamma}_0$ representation), $\Delta\lambda/\lambda$ depends only on the second moment about the

center of mass and it can be obtained by the application of (7). Therefore, we resorted to the $\mathbf{\Gamma}_0$ eigenvalues and estimated the full second-moment matrix of the images. Since the dark noise limits the accuracy of the $\mathbf{\Gamma}_0$ calculation by sums over the pixels (the noise in the tails has the heaviest weight and errors in identifying and subtracting it yield oversized or undersized estimates), the pixels far from the center of mass can be advantageously discarded [20]. Attention was given to the trade-off between clipping and noise rejection; but, as part of the spectrum is rejected too, there were unavoidable subjectivity and uncertainty. Therefore, in [15, 16], we estimated $\mathbf{\Gamma}_0$ by fitting the bivariate Gauss function

$$\hat{I}(\boldsymbol{\theta}) + C = A \exp(-\boldsymbol{\theta}^T \mathbf{\Gamma}_0^{-1} \boldsymbol{\theta} / 2) + C \quad (8)$$

to the focal plane data $I_{\text{FP}}(\boldsymbol{\theta}_i)$. The results are shown in figures 1 and 2.

The PTB developed a procedure to obtain the angular spectrum via the discrete Fourier transform of two-dimensional samples of the complex amplitude estimated from wavefront and intensity profiling by means of a Shack–Hartmann sensor [15]. In this case, the intensity and wavefront samples are fitted by using bivariate Gauss functions (intensity samples) and Zernike polynomials (wavefront samples) as bases. Next, the results are combined to give the complex amplitude, which

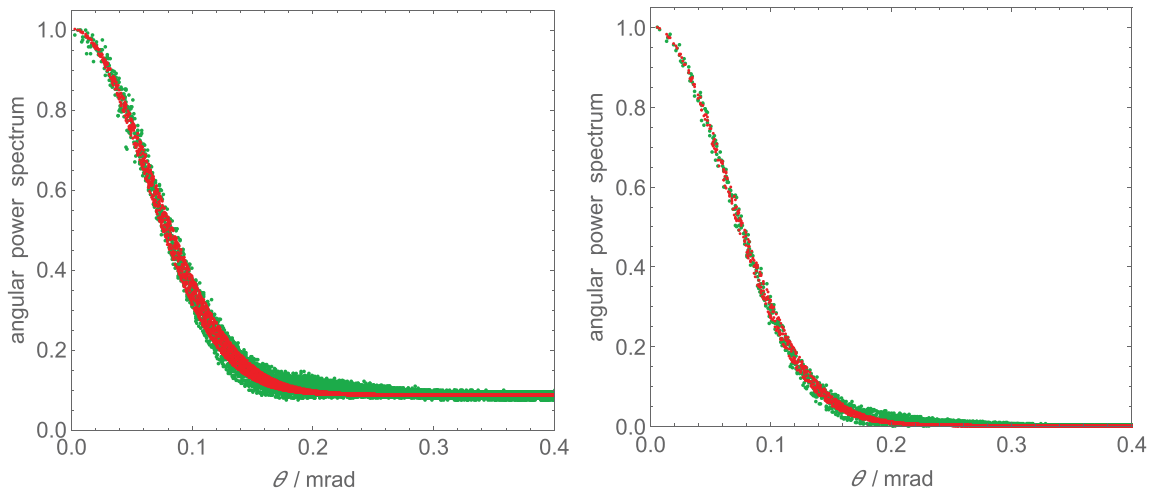


Figure 2. Green dots: radial plot of the focal plane images shown in figure 1. Red: bivariate Gauss functions fitting the data. Left: February 2014 measurement, COHU 6710 camera. Right: May 2014 measurement, HAMAMATSU FLASH 4.0 camera.

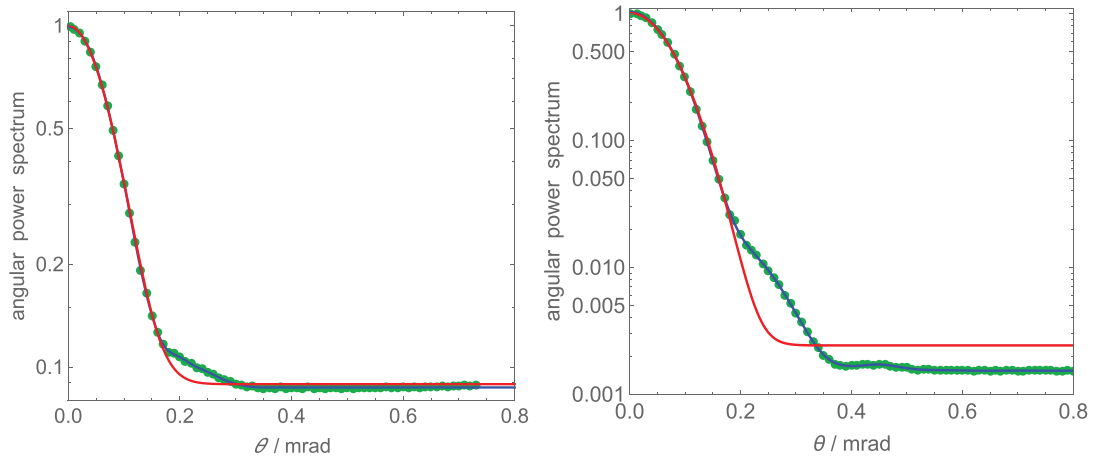


Figure 3. Green dots: radial (logarithmic) plot of the focal plane images shown in figure 1. The radial bins are 10 μ rad wide. Left: February 2014 measurement, COHU 6710 camera. Right: May 2014 measurement, HAMAMATSU FLASH 4.0 camera. Gauss functions (red) and (9a) and (9b) models (blue) fitting the data are also shown.

is re-sampled to calculate the angular spectrum by discrete Fourier transform. Owing to the data smoothing, the spectrum is free of noise, so that the mass center and second moments can be obtained from sums over the samples.

A comparison of the INRIM and PTB power-spectrum measurements, done by means of travelling standards realized in the form of single-mode fibers equipped with collimators, brought into evidence that the INRIM’s smoothing of the focal-plane images by Gauss functions was unable to take small spectrum components at relatively large angles into account. As shown in figure 2 and [16], this problem went unnoticed, but it is brought into light by the logarithmic plots shown in figures 3 and 4.

In order to eliminate the difficulty of capturing these components by fitting analytically-specified freeform shapes to the two-dimensional images, the PTB rethought about the problem and realized that it can be made one-dimensional as shown in (7). Since the impact of noise is reduced in the processing, $\mathcal{I}(\theta)$ can be approximated binning the pixels having the same (rounded) radial coordinate. The integration over the radial direction is done by fitting

$$\hat{\mathcal{I}}(\theta) + C = e^{-Q\theta^2} \left[\sum_{i=1}^n A_i L_i(Q\theta^2) \right]^2 + C, \quad (9a)$$

where the Gauss–Laguerre functions are used as basis, to the binned data, $\mathcal{I}_{FP}(\theta_i)$. When the spectrum components to be modelled are many orders of magnitude smaller than the spectrum peak, it is convenient to fit

$$\theta^2 \hat{\mathcal{I}}(\theta) + C\theta^2 = \theta^2 e^{-Q\theta^2} \left[\sum_{i=1}^n A_i L_i(Q\theta^2) \right]^2 + C\theta^2 \quad (9b)$$

to the $\theta_i^2 \mathcal{I}_{FP}(\theta_i)$ data. Figures 3 and 4 show the binned data and compares (9a) and (9b) against Gauss functions. It is worth noting that (9a) and (9b) are tools to remove the dark noise, to smooth the binned data and to ensure that $\hat{\mathcal{I}}(\theta) > 0$ and that the integrals in the trace calculation converge and are insensitive to the dark noise. From a physical viewpoint, (9a) and (9b) model effective beams having the same central second-moment, but cylindrical symmetry. Figure 5 shows the

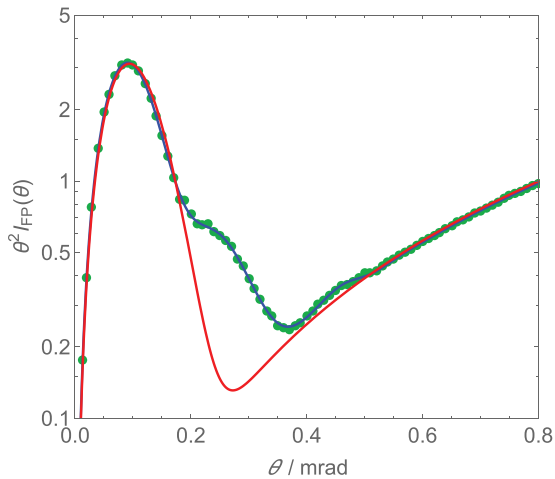


Figure 4. Green dots: radial (logarithmic) plot of the $\theta_i^2 \mathcal{I}_{FP}(\theta_i)$ data shown in figure 3 (right). The radial bins are 10 μ rad wide. The Gauss function (red) and (9b) model (blue) fitting the data are also shown.

convergence of the $\text{Tr}(\mathbf{\Gamma}_0)$ estimate with respect to the number n of basis functions.

The initial estimate of the beam-axis direction is found by the fitting of a bivariate Gauss function to the data. Since the trace of the non-central second-moment matrices,

$$\text{Tr}(\mathbf{\Gamma}_1) = \text{Tr}(\mathbf{\Gamma}_0) + |\boldsymbol{\theta}_1 - \boldsymbol{\theta}_0|^2, \quad (10)$$

where $\boldsymbol{\theta}_1$ is any direction, exceed $\text{Tr}(\mathbf{\Gamma}_0)$ by the square of the $\boldsymbol{\theta}_1$ distance from the beam axis direction $\boldsymbol{\theta}_0$, the center uncertainty propagates into an overestimate. It is worth noting that $\beta_1 = |\boldsymbol{\theta}_1 - \boldsymbol{\theta}_0|$ is the angular misalignment between the beam axis and the $\boldsymbol{\theta}_1$ direction. Therefore, if the displacement occurs along $\boldsymbol{\theta}_1$, the $\text{Tr}(\mathbf{\Gamma}_1)/2$ error includes the $\beta_1^2/2$ contribution of (5). This brings into light that the splitting of the fringe-period error in diffraction and cosine contributions is conventional. Equation (10) suggests to improve the correction estimate by minimizing the trace calculation versus the non-centrality of the second moment. As it is shown in figure 6, this is done by fitting the

$$\text{Tr}[\mathbf{\Gamma}(\theta_x, \theta_y)] = a_0 + a_x \theta_x + a_y \theta_y + (\theta_x^2 + \theta_y^2) \quad (11)$$

parabola to the traces of a number of non-central moments.

5. Results

The table 1 compares the old and new diffraction corrections obtained by fitting bivariate Gauss functions (2010 and 2014) and models (9a) and (9b) (2017) to the focal plane images of the beams exiting from the INRIM’s combined x-ray and optical interferometer. In 2010, to check the measurement procedure, the INRIM used different fiber collimators. In 2014, to investigate the beam clipping by the interferometer optics and the difference between the two interfering beams, the power-spectrum measurements were carried out separately on both the reference and measurement beams (May 2014, analyser side B) and with a variable iris in the optical path (February 2014, analyser side A).

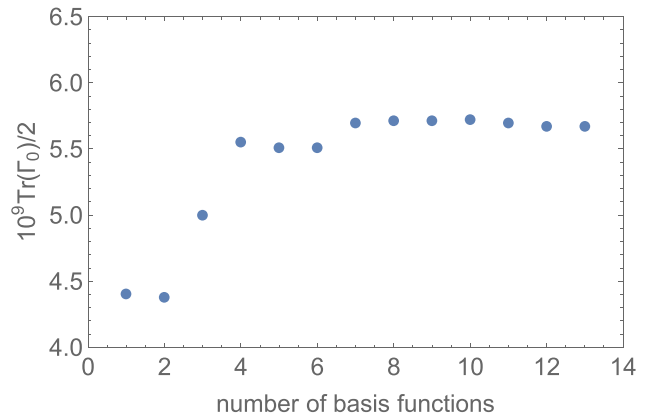


Figure 5. $\text{Tr}(\mathbf{\Gamma}_0)/2$ estimate from the data shown in figure 4 versus the number n of basis functions in (9b).

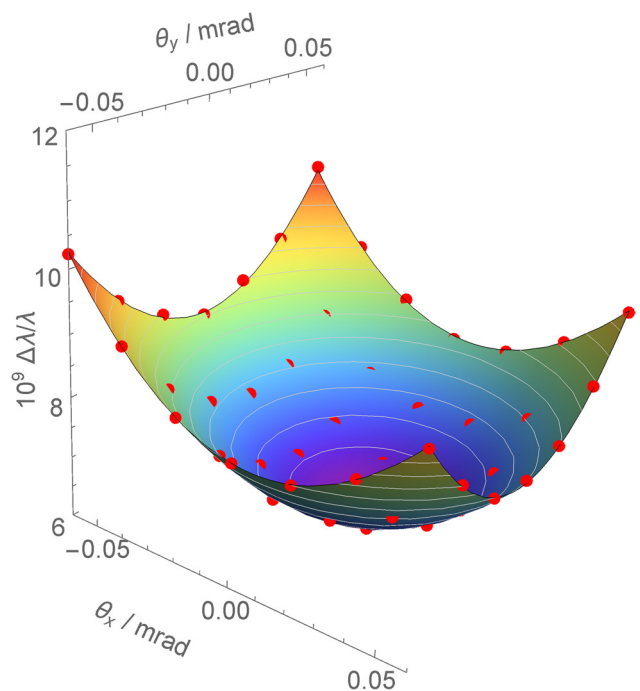


Figure 6. Diffraction error versus the non-centrality of the second moment. The red dots are the non-central moments of the focal plane image shown in figure 1 (top). The paraboloid fitting the data is also shown; the minimum coordinates indicate the propagation direction of the beam.

In 2010, the measured values of the lattice parameter carried out with the analyser assembled in the front (side A) and inverted (side B) layouts were separately corrected; in 2014, all the measured values were corrected for the same, average, error. The new corrections values have been obtained by reexamining the archive files of the angular power-spectrum measurements and by recalculating the second central moments. All the corrections were obtained by minimizing the trace calculation versus the non-centrality of the second moment.

Four terms contribute to the correction uncertainty: the calibration of the focal plane coordinates, the focus of the autocollimator and telescope, the integration of the noisy data points, and scattering by dust particles in the beam path.

Table 1. Diffraction correction, expressed in nm m^{-1} , calculated by fitting the focal plane images of the beam with Gauss functions (2010 and 2014) and the model (9a) and (9b) (2017). To allow the lattice parameter values published in 2011 [15] and 2015 [16] to be re-corrected, the new corrections are given (2017), together with the ones applied in 2010 and 2014.

Data file	$\Delta\lambda/\lambda$ 2010	$\Delta\lambda/\lambda$ 2017	Data file	$\Delta\lambda/\lambda$ 2014	$\Delta\lambda/\lambda$ 2017
Analyser side A					
Collimator 12 mm ^a	7.16	8.17	Iris 9 mm ^a	3.89	5.45
Collimator 12 mm ^a	7.16	8.29	Iris 9 mm ^a	3.94	5.42
Collimator 12 mm ^b	7.36	7.51 ^d	Iris 10 mm ^a	3.84	4.92
			Iris 10 mm ^a	3.84	5.27
Old and New correction	7.26(65)	8.2(1.2) ^d			
Analyser side B					
Collimator 15 mm ^a	8.93	15.56	Interfering beams ^c	4.08	6.13
			Interfering beams ^c	4.15	5.64
			Reference beam ^c	4.00	6.26
			Measure beam ^c	4.00	5.94
Old and new correction	8.93(85)	15.6(2.3)			
Old and new correction				3.97(60)	5.63(85)

^a Hilger and Watts TA3 autocollimator and COHU 6710 camera.

^b Converging lens and COHU 6710 camera.

^c Converging lens and HAMAMATSU FLASH 4.0 camera.

^d Owing to a non-optimized beam intensity, only the Gaussian tip of the angular power-spectrum is detectable. Therefore, this value was excluded from the 2017 average.

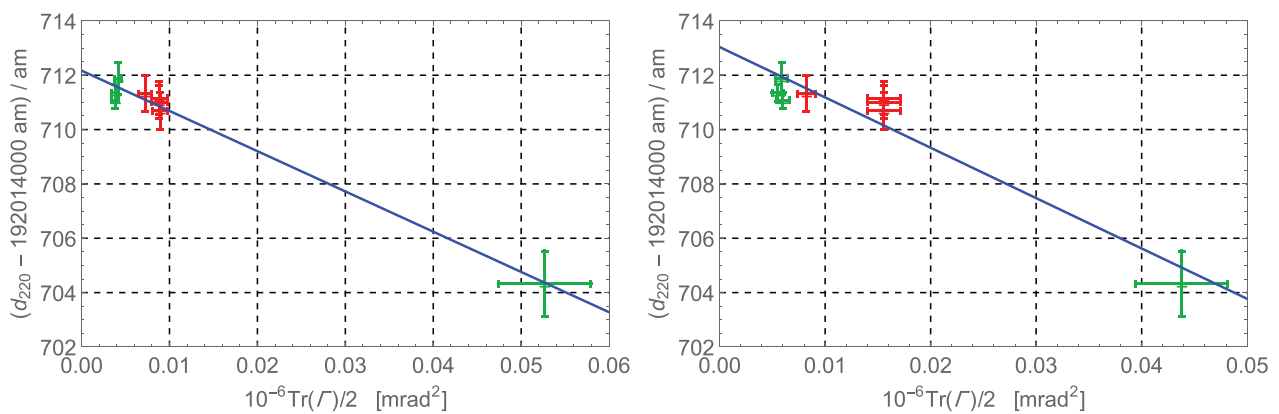


Figure 7. Measured values of the ^{28}Si lattice parameter versus the correction for the laser-beam diffraction. The measurements were made from 2010 to 2014. Red: 633 nm He–Ne laser. Green: 532 nm frequency-doubled Nd:YAG laser. Left: focal plane data fitted with Gauss functions. Right: focal plane data fitted with (9a) and (9b) models. Blue: best lines fitting the data.

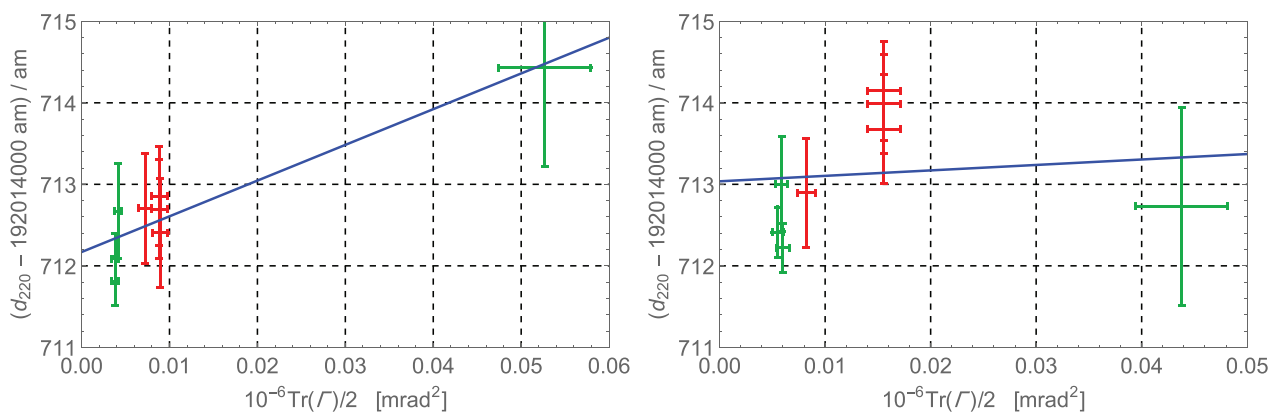


Figure 8. Corrected lattice parameter values versus the applied correction. The measurements were made from 2010 to 2014. Red: 633 nm He–Ne laser. Green: 532 nm frequency-doubled Nd:YAG laser. Left (reproduced from [16]): focal plane data fitted with Gauss functions. Right: focal plane data fitted with (9a) and (9b) models. Blue: best lines fitting the data.

The uncertainty of the focal plane calibration is 4%. The fractional error due to a detection offset $\sigma_z \approx 2$ mm with respect to the focal plane is

$$\frac{\sigma_{\text{Tr}}}{\text{Tr}(\mathbf{\Gamma})} \approx \frac{2|F - z_0|\sigma_z}{F^2}, \quad (12)$$

where $F = 0.5$ m is the focal length and z_0 the distance of the beam waist from the lens principal plane. We don't know exactly is the beam waist, but assuming $|F - z_0| \approx 3$ m, which is compatible with the size of the experimental set-up, the fractional uncertainty is 5%. As regards the momentum calculation, the observed variability associated to different binning of the power-spectrum samples and the number of basis functions is about 5%. Though this uncertainty is reduced by the averaging over different binnings implied by the momentum minimization, we nevertheless maintained the 5% fractional uncertainty. Eventually, the last source of uncertainty is the forward scattering by dust particles. Putting it all together, we cautiously associated to the 2017 corrections given in table 1 a fractional uncertainty equal to 15%.

In [16], to check the correction estimate, we examined the results of a number of test d_{220} measurements carried out from 2010 to 2014 with different laser beams. The measurement results are shown in figure 7 together with the relevant correction for the diffraction. The corrected values given in [16] and reproduced in figure 8 (left) suggested overestimated corrections, but we were unable to shed light on the problem. All the archive files of the angular power-spectrum measurements made at the time were reexamined and the second central moments recalculated by fitting (9a) and (9b) to the focal plane data. Though these test measurements were not explicitly carried out to study diffraction and not all of them own a full experimental check of the error budget, the results given in figures 7 and 8 (right) show that the supposed overestimate disappears and confirm the improvement achieved.

6. Conclusions

An error was found in the estimate of the correction for the laser-beam diffraction of the INRIM measurements of the ^{28}Si lattice parameter by combined x-ray and optical interferometry [15, 16]. Specifically, the correction—which is proportional to the second central moment of the angular power-spectrum—was calculated as relevant to the bivariate Gaussian-beam that most closely approaches the measured spectrum. However, small spectrum components at large angles went unnoticed, but they had a significant effect on the momentum.

The archived measurements of the angular power-spectrum were reexamined and the second central moments recalculated by exploiting symmetries to filter the noise and to reduce the calculation to a one-dimensional integration. This allowed for high-order analytical approximations of the one-dimensional data and more accurate momentum calculations. To allow the lattice parameter values given in [15, 16] to be re-corrected,

the newly calculated corrections have been given, together with the applied ones.

The results obtained bring into light the importance of beam characterization when calibrating wavelength standards for optical interferometry. The transposition of the frequency uncertainty into the wavelength one might lead to underestimations; high-accuracy measurements or poor beam quality might also require the specification of the beam angular spectrum.

Acknowledgments

We thank the late Alain Picard who, dissatisfied by our explanations of the data in figure 8, kept alive the need to pursue the matter. This work was partly funded by the Italian ministry of education, university, and research (project P6-2013, implementation of the new SI).

ORCID

G Mana  <https://orcid.org/0000-0002-4109-7254>

References

- [1] Dorenwendt K and Boensch G 1976 *Metrologia* **12** 57
- [2] Mana G 1989 *Metrologia* **26** 87
- [3] Bergamin A, Cavagnero G and Mana G 1994 *Phys. Rev. A* **49** 2167–73
- [4] Bergamin A, Cavagnero G, Cordiali L and Mana G 1997 *IEEE Trans. Instrum. Meas.* **46** 196–200
- [5] Bergamin A, Cavagnero G, Cordiali L and Mana G 1999 *Eur. Phys. J. D* **5** 433–40
- [6] van Westrum D and Niebauer T M 2003 *Metrologia* **40** 258
- [7] Cavagnero G, Mana G and Massa E 2006 *J. Opt. Soc. Am. A* **23** 1951–9
- [8] Robertsson L 2007 *Metrologia* **44** 35
- [9] D'Agostino G and Robertsson L 2011 *Appl. Phys. B* **103** 357–61
- [10] Andreas B, Ferroglio L, Fujii K, Kuramoto N and Mana G 2011 *Metrologia* **48** S104
- [11] Andreas B, Fujii K, Kuramoto N and Mana G 2012 *Metrologia* **49** 479
- [12] Andreas B, Mana G and Palmisano C 2015 *J. Opt. Soc. Am. A* **32** 1403–24
- [13] Andreas B, Mana G and Palmisano C 2016 *J. Opt. Soc. Am. A* **33** 559–60
- [14] Sasso C P, Massa E and Mana G 2016 *Opt. Express* **24** 6522–31
- [15] Massa E, Mana G, Kuetgens U and Ferroglio L 2011 *Metrologia* **48** S37
- [16] Massa E, Sasso C P, Mana G and Palmisano C 2015 *J. Phys. Chem. Ref. Data* **44** 031208
- [17] Mana G et al 2015 *J. Phys. Chem. Ref. Data* **44** 031209
- [18] Day G W and Stubenrauch C F 1978 *Natl. Bur. Stand. Techn. Note* 1001
- [19] Goodman J 1996 *Introduction to Fourier Optics (McGraw-Hill Series in Electrical and Computer Engineering: Communications and Signal Processing)* (New York: McGraw-Hill)
- [20] Mana G, Massa E and Rovera A 2001 *Appl. Opt.* **40** 1378–85